

Physics-informed Neural Model Predictive Control of Interacting Active Brownian Particles

Titus Quah,¹ Sho C. Takatori,² and James B. Rawlings¹

¹*Department of Chemical Engineering, University of California–Santa Barbara, Engineering II Building, Santa Barbara, CA 93106*

²*Department of Chemical Engineering, Stanford University, 443 Via Ortega, Stanford, CA 94305*
(Dated: February 3, 2025)

Active matter systems, composed of self-propelled agents that convert energy into directed motion, exhibit a wide range of emergent behaviors, such as motility-induced phase separation, flocking, and swarming. These phenomena, observed across natural and engineered systems, hold immense potential for applications in programmable materials, directed assembly, and micro-robotics. However, precisely controlling their macroscopic continuum fields, e.g., density or flux, remains a significant challenge due to the complexity of multibody interactions and correlated particle dynamics. To address this challenge, we present a framework that combines physics-informed machine learning with Model Predictive Control. Our approach learns a closure model for complex particle interactions while incorporating known physical principles, resulting in an accurate predictive model suitable for real-time control. By integrating this model into a Model Predictive Control framework, we enable systematic optimization of control actions that can guide the system toward desired macroscopic behaviors. Through two illustrative examples, we showcase the versatility of the framework. First, we control the spatial distribution of particles by splitting them into two groups and dynamically juggling their densities. Second, we simultaneously control both the number density and the mean flux, guiding the latter to follow a prescribed sinusoidal profile. These results highlight the framework’s potential to systematically control complex dynamics in active matter systems and provide a foundation for broader applications in programmable and adaptive materials.

I. INTRODUCTION

Active matter systems consist of self-propelled particles that convert energy into directed motion, leading to a wide range of emergent phenomena [1–5]. These include motility-induced phase separation (MIPS), flocking, and swarming, observed across various natural and synthetic systems such as bacterial colonies, bird flocks, and micro-robots[6–9]. Understanding and harnessing these emergent behaviors have the potential to revolutionize applications in programmable materials, directed assembly, and micro-robotics [10–14].

To achieve these goals, researchers have developed actuation strategies for active matter systems using external fields like magnetic, optical, acoustic, and electric stimuli[15–26]. Despite advancements in actuation, systematic control of emergent behaviors in active matter systems remains a significant challenge. Early efforts in control focused on heuristic approaches and reinforcement learning to navigate and manipulate these systems [25, 27–33]. However, these strategies lack scalability to interacting systems where there are many degrees of freedom. Another approach employs optimality conditions to derive Euler-Lagrange equations, which are solved using adjoint methods [34–39]. While these methods offer precision, their computational demands make real-time feedback control challenging, further highlighting the need for scalable and adaptive control strategies.

To address the limitations of computationally demanding methods for real-time feedback control, Model Predictive Control (MPC) offers a scalable and adaptive alternative. By discretizing the system dynamics and solving a nonlinear optimization problem at every sam-

ple time, MPC incorporates feedback and handles constraints effectively. This enables real-time control, allowing the system to adapt to disturbances and model inaccuracies [40]. MPC’s versatility has been demonstrated across domains such as chemical processes, robotics, and flow control [41–43]. However, applying MPC to active matter systems at the continuum level is hindered by the lack of an accurate predictive model, which is critical for leveraging MPC’s full potential. The challenge lies in capturing the complexity of active matter interactions, such as multibody dynamics and hydrodynamic coupling. Previous approaches rely on phenomenological models that capture the phenomena qualitatively or approximations and simplifications like quasi-equilibrium approximation of the distribution function or closures that apply to specific geometries [44–48]. Addressing these modeling gaps is essential for realizing robust and efficient control of emergent behaviors in active matter systems.

One promising approach to overcoming this challenge is physics-informed machine learning (PIML). PIML combines data-driven techniques with physical models to learn governing equations from limited data, ensuring both accuracy and generalizability [49–52]. In the realm of active matter, PIML has been used to discover equations for active nematics and chiral active Brownian particles (ABPs) as well as learn closures for active fluids [53–57]. By leveraging the strengths of PIML, we propose a gray-box modeling framework that integrates known physical principles with machine learning to develop predictive models suitable for MPC. This framework, which has shown promise in controlling drones,

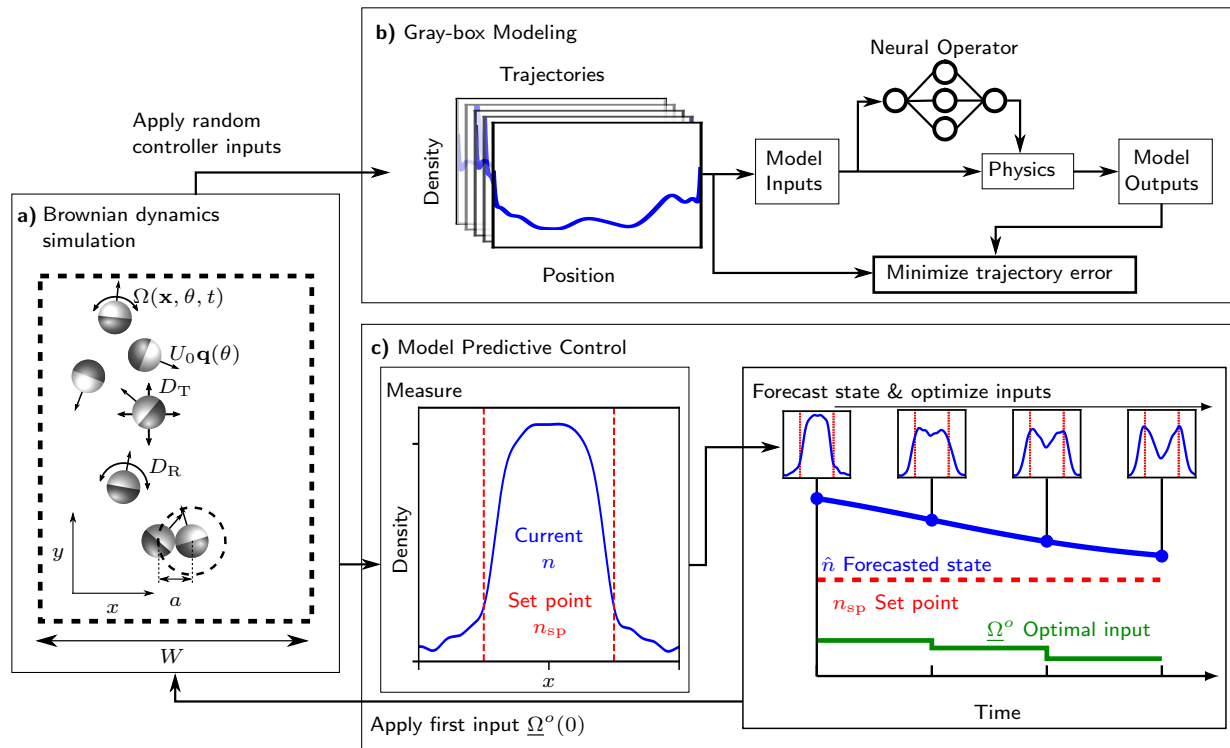


FIG. 1. Physics-informed machine learning framework for modeling and control of interacting active matter. (a) Schematic of interacting active Brownian particles (ABPs) in 2D. The particles exhibit complex dynamics due to multibody interactions and correlated particle behavior. As a case study, in this work we use Brownian dynamics simulations of active particles with controllable angular velocities from a spatiotemporal external torque. More generally, our framework may be applied to systems where the particle density is observable or can be estimated, including microscopy images of controllable active particles. (b) The gray-box modeling framework combines physics-informed machine learning with a neural operator to learn a closure model for multibody interactions, enabling the prediction of density dynamics. The predictive model is trained to align closely with observed system behavior, leveraging past state and input data. (c) The gray-box model is integrated into a Model Predictive Control (MPC) framework, where it is used to control emergent behaviors. MPC optimizes the control inputs to achieve user-defined objectives, such as splitting the particle population into groups or dynamically controlling fluxes. Our framework can handle complex particle interactions and optimize control actions for precise and adaptive manipulation of active matter.

chemical reactors and heating, ventilation, and air conditioning systems [58–60], offers a pathway to systematically control the emergent behaviors of active matter systems while addressing the challenges posed by their complex dynamics.

We demonstrate the proposed framework on a system of interacting ABPs, as shown in Fig. 1a. A key challenge in active matter research is handling the complexity of multibody interactions and correlated particle dynamics. Using physics-informed machine learning, i.e., gray-box modeling, we learn a closure model for these interactions, and obtain a predictive model that aligns with observed system behavior (Fig. 1b). This predictive model is then integrated into an MPC framework, enabling the systematic control of emergent behaviors (Fig. 1c).

We validate the framework through two illustrative examples. In the first example, we split the particle population into two groups and dynamically juggle densities

between the groups, showcasing the ability to achieve precise spatial and temporal control of number densities. In the second example, we simultaneously control both the number density and the mean flux, guiding the mean flux to follow a prescribed sinusoidal profile. Here, the controller adjusts particle alignment and external fields to regulate the mean flux while ensuring that the particle groups remain concentrated at their target positions. These examples demonstrate the framework’s effectiveness in both learning complex dynamics and optimizing control actions, paving the way for broader applications in active matter systems.

II. BROWNIAN DYNAMICS SIMULATION

We consider a system of N interacting ABPs in two spatial dimensions as shown in Fig. 1a. In addition, the particles’ orientations can be manipulated via a spatiotemporally-varying actuated field that induces an

angular velocity. The dynamics of particle i with center of mass position $\mathbf{x}_i = [x_i \ y_i]^T$, orientation $\mathbf{q}_i = [\cos(\theta_i) \ \sin(\theta_i)]^T$ and orientation polar angle θ_i , where $i = 1, \dots, N$, can be described by the following Brownian dynamics equations, where the overdot denotes a time derivative:

$$\dot{\mathbf{x}}_i = U_0 \mathbf{q}_i + \nu_{\text{int},i} + \sqrt{2D_T} \mathbf{W}_{T,i}(t) \quad (1)$$

$$\dot{\theta}_i = \Omega_i + \sqrt{2D_R} W_{R,i}(t), \quad (2)$$

Here, U_0 represents the self-propulsive speed; the interaction term $\nu_{\text{int},i}$ takes the form $\nu_{\text{int},i} = -(D_T/k_B T) \sum_{j=1, j \neq i}^N \nabla_i U_2(\|\mathbf{x}_i - \mathbf{x}_j\|)$; D_T is the translational diffusion coefficient; $k_B T$ is the thermal energy scale; The gradient operator with respect to \mathbf{x}_i is denoted as $\nabla_i = \left[\frac{\partial}{\partial x_i} \ \frac{\partial}{\partial y_i} \right]^T$; The two-particle interaction potential $U_2(\|\mathbf{x}_i - \mathbf{x}_j\|)$ governs particle interactions, with $\|\cdot\|$ denoting the Euclidean norm; The actuated spatiotemporal-varying field induces an angular velocity $\Omega_i = \Omega(\mathbf{x}_i, \theta_i, t)$; $D_R = 3D_T/a^2$ represents the rotational diffusion coefficient, where a is the particle diameter; Thermal fluctuations are modeled through Wiener processes $\mathbf{W}_{T,j}(t)$ and $W_{R,j}(t)$ with zero-mean and unit variance white noise statistics.

For particle interactions, we employ the Weeks-Chandler-Andersen potential: $U_2(r) = 4\epsilon \left[\left(\frac{a}{r}\right)^{12} - \left(\frac{a}{r}\right)^6 \right] H(2^{1/6}a - r)$, where ϵ represents the interaction strength, r denotes the particle separation distance, and $H(\cdot)$ is the Heaviside step function. The actuated field aligns particles in the x direction according to $\Omega(\mathbf{x}, \theta, t) = -\Omega_x(x, t) \sin(\theta)$, where positive values of Ω_x promote alignment in the $+x$ direction and vice versa. The field maintains uniformity in y and is constrained to be periodic in x with period W and maximum magnitude Ω_{max} , such that $\|\Omega_x(\mathbf{x}, t)\|_{\infty} \leq \Omega_{\text{max}}$.

We nondimensionalize Eqs. (1) and (2) using the rotational diffusion time $\tau_R = 1/D_R$, run length $\ell = U_0 \tau_R$, and thermal energy $k_B T$ as our fundamental units. This yields two key dimensionless parameters: the ratio of run length to microscopic diffusion length $(\ell/\delta)^2 = U_0^2 \tau_R / D_T$, where $\delta = \sqrt{D_T / \tau_R}$, and the area fraction $\phi = \bar{n} \pi a^2 / 4$, with \bar{n} representing the spatially averaged particle number density.

For our simulations, we set $N = 10^4$, $(\ell/\delta)^2 = 100$, $\phi = 0.4$, $W = 10\ell$, and $\Omega_{\text{max}} = 3\tau_R$. The simulation width is set to W to match the actuator periodicity, and the height is adjusted to ensure the correct area fraction. Under these conditions, the system exhibits motility induced phase separation (MIPS) in the absence of an actuating field [61]. The dynamics are simulated using HOOMD-blue [62].

III. GRAY-BOX MODEL FOR THE NUMBER DENSITY

We wish to control the x -number density $n(x, t)$, which

is the the one-particle distribution function $P(\mathbf{x}, \theta, t)$ marginalized over orientation θ and spatial dimension y :

$$n(x, t) = \int \int P(\mathbf{x}, \theta, t) d\theta dy \quad (3)$$

x and y are the spatial dimensions; $\mathbf{x} = [x \ y]^T$; θ is the orientation angle; The x -number density $n(x, t)$ is a macroscopic property that characterizes the spatial distribution of particles and is measurable in experiments.

The control strategy employs MPC to determine an optimal sequence of actuating fields Ω^o that drives the number density $n(x, t)$ toward a user-specified set point $n_{\text{sp}}(x, t)$, as illustrated in Fig. 1c. Anticipating that system perturbations and model uncertainties will cause deviations between the predicted and realized trajectories, we incorporate feedback control to adjust the actuating field accordingly. Our implementation operates under the constraint that feedback is available only through measurements of the number density $n(x, t)$, taken at discrete time intervals h .

To proceed with MPC, we require a predictive dynamical model for $n(x, t)$. Rigorously, one could begin with the N -body Smoluchowski equation and account for binary interactions with an interaction potential that depends only on the particle separation distance:

$$\dot{P}_N(\mathbf{X}, t) + \sum_{i=1}^N \nabla_i \cdot \mathbf{j}_i + \frac{\partial}{\partial \theta_i} j_{R,i} = 0 \quad (4)$$

$$\mathbf{j}_i = U_0 \mathbf{q}_i P_N(\mathbf{X}, t) - D_T \nabla_i P_N(\mathbf{X}, t) + \nu_{\text{int},i} P_N(\mathbf{X}, t) \quad (5)$$

$$j_{R,i} = \Omega_i P_N(\mathbf{X}, t) - D_R \frac{\partial}{\partial \theta_i} P_N(\mathbf{X}, t) \quad (6)$$

$P_N(\mathbf{X}, t)$ is the N -particle distribution function; $\mathbf{X} = [\mathbf{x}_1^T, \dots, \mathbf{x}_N^T, \theta_1, \dots, \theta_N]^T$ denotes the collection of the particles' positions and orientations; \mathbf{j}_i and $j_{R,i}$ are the translational flux and rotational flux associated with particle i , respectively.

The traditional approach of integrating over $N - 1$ particle positions and orientations yields the Bogouilubov-Born-Green-Kirkwood-Yvon (BBGKY) hierarchy, where the one-particle distribution function $P_1(\mathbf{x}, \theta, t)$ depends on the two-particle distribution function $P_2(\mathbf{x}_1, \theta_1, \mathbf{x}_2, \theta_2, t)$ and so on. The primary challenge lies in determining a closure relation that links higher-order distribution functions to lower-order ones [45, 63, 64]. One closure strategy is to rewrite the two-particle distribution function in terms of the pair-distribution function. Assuming weakly varying external fields, the pair-distribution function can be learned using data from microscopic simulations [65, 66]. This reduces the hierarchy to focus on the one-particle distribution function.

To make further progress with the one-particle distribution function, it is often expanded as a series of orientational moments, such as density, polar order, nematic

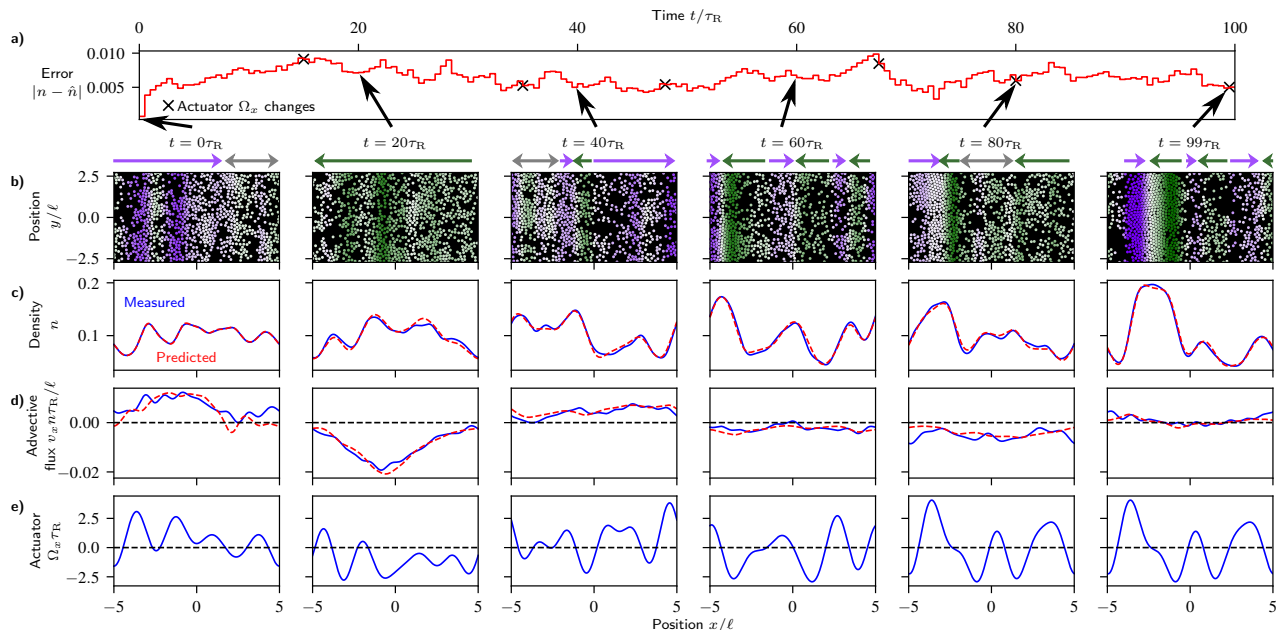


FIG. 2. Prediction accuracy of the gray-box model over a $100 \tau_R$ time horizon using testing data. (a) The L^2 norm of the error between the predicted and measured number densities remains below 0.01 throughout the simulation, indicating a close match to the true number density profile. X-marks indicate points where the actuator field changes. (b) Snapshots of the particle simulation are shown for six time points: $t = [0\tau_R, 20\tau_R, 40\tau_R, 60\tau_R, 80\tau_R, 99\tau_R]$. Particles are colored based on their polar order in the x direction, normalized by density, $m_x(x)/n(x)$, where $m_x(x) = \int \int \cos(\theta) P(\mathbf{x}, \theta, t), d\theta, dy$. Positive polar order (particles oriented to the right) is shown in purple, while negative polar order (particles oriented to the left) is shown in green. Regions without strong polar order are colored white. Colored arrows above the particles are included for visual clarity. (c) Snapshots of the number density field for both measured (blue) and predicted (red) values are shown for the same six time points as in (b). (d) The advective flux due to the velocity field $v_x n$ is displayed for measured (blue) and predicted (red) values, with fluctuations attributed to particle collisions. (e) The actuating field applied during the simulation is shown for context.

order, and higher-order terms [64]. This expansion typically requires an additional moment closure to truncate the series. By assuming that the polar order dominates over higher-order moments and that it is quasi-stationary with respect to density changes, one arrives at a density-only active Model B+ [45].

In our work, we aim to achieve closure at the density level only while accounting for external fields that may vary significantly in both space and time. Furthermore, unlike prior analytical work using the moments expansion, our density field evolution equation is formulated to capture deep higher-order moments, far beyond the polar order, even when the density is not the dominant term. As a proof of concept, we focus on the number density, i.e. the zeroth orientational moment. The dynamics of this quantity can be described by an advection-diffusion equation:

$$\dot{n}(\mathbf{x}, t) + \nabla \cdot (-D_T \nabla n(\mathbf{x}, t) + \mathbf{v}(\mathbf{x}, t)n(\mathbf{x}, t)) = 0 \quad (7)$$

$\mathbf{v}(\mathbf{x}, t)$ represents the effective velocity field that encompasses self-propulsion, multibody particle interactions, and the actuated field.

By writing Eq. (7), we are “closing” the moments expansion at the zeroth moment (the density), but capturing all higher-order moments via the advective term,

$\mathbf{v}(\mathbf{x}, t)$. This is the key concept that differentiates our gray-box model from prior analytical moments expansion approaches. Similar to learning the pair-distribution function, our goal is to use data from particle-based simulations and experiments to learn $\mathbf{v}(\mathbf{x}, t)$ without directly dealing with the interactions terms and higher-order couplings analytically. At the end of the day, we end up with a single advection-diffusion equation that can be used in various applications, including optimal control. While an exact mapping between measured number densities, actuator inputs, and their past values to this effective velocity field would enable MPC, such a mapping is not readily available. To these ends, we employ a physics-constrained, data-driven (gray-box) approach to learn $\mathbf{v}(\mathbf{x}, t)$. This method draws parallels to stochastic force inference, where we learn an effective force from stochastic simulations that captures the combined effects of interparticle interactions, external fields, and self-propulsion [67]. The resulting inferred model provides both predictive accuracy and a foundation for implementing MPC to control emergent behaviors.

A. Gray-box model formulation and training

As a test case, we demonstrate the application of the gray-box model to learn the x -number density dynamics

for a system of interacting ABPs in 2D, where variations in y are integrated out, leaving a 1D density that varies only in x . The gray-box model is expressed as:

$$\frac{\partial \hat{n}(x, t)}{\partial t} + \frac{\partial}{\partial x} \left(-D_T \frac{\partial}{\partial x} \hat{n}(x, t) + \hat{v}_x(x, t) \hat{n}(x, t) \right) = 0 \quad (8)$$

$$\hat{v}_x(x, t) = v_{\text{NN}}(\hat{n}(x, t), \Omega_x(x, t), p(x, t); \beta_{\text{NN}}) \quad (9)$$

where $\hat{n}(x, t)$ and $\hat{v}_x(x, t)$ are the predicted number density and velocity fields, respectively; The neural operator $v_{\text{NN}}(\cdot)$ approximates the effective velocity field; $p(x, t)$ contains N_p past number density and actuator fields, and β_{NN} representing the neural operator parameters. Since we only model number density dynamics without access to higher-order moments (e.g., polar order or the two-particle distribution function), we incorporate past state and input values $p(x, t)$ to approximate these unmeasured states, following Taken's embedding theorem [68]. Through the advection-diffusion structure, this formulation ensures mass conservation and non-negative densities.

Given our discrete-time measurements with interval h , we hold the actuator constant between each measurement time and integrate Eq. (8) using spectral methods and method of lines with time step h to derive the discrete-time dynamics $f_h(\cdot)$:

$$\hat{n}(k+1) = f_h(\hat{n}(k), \Omega_x(k), v_{\text{NN}}(\hat{n}(k), \Omega_x(k), p(k); \beta_{\text{NN}})) \quad (10)$$

k denotes the discrete time index. We omit the spatial dependence in x for brevity. To determine the neural operator parameters β_{NN} , we collect number density trajectories by applying random controller input sequences following the protocol in Appendix A 2. Briefly, we performed 2D periodic BD simulations of interacting ABPs, applying random spatial collocation of actuated control torques in 1D over randomly selected time durations. The x -number density is represented in a spectral basis and estimated from particle positions through orthogonal series estimation, as detailed in Appendix A 5 [69]. To capture both transient and steady-state dynamics, the actuated torque field was held constant over random intervals, allowing the ABPs to sample diverse configurations. Using the initial frames to set $\hat{n}(x, 0)$ and $p(x, 0)$, we generate predicted trajectories and optimize β_{NN} to minimize the discrepancy between measured and predicted trajectories, as illustrated in Fig. 1b.

We set the sampling time to $h = 0.5\tau_R$ and utilize $N_p = 2$ past fields. Our dataset spans $10^4\tau_R$, encompassing nearly 2000 unique inputs. The implementation leverages PyTorch for the neural operator architecture, employs a modified Backward Euler method for discrete-time dynamics, and utilizes the Adam optimizer for loss minimization. Since the density field dynamics evolve on a slower time scale than the discrete Langevin particle dynamics, we are able to take large time steps in our implicit solver. Detailed training protocols are documented

in Appendix A 4.

B. Model validation

Fig. 2 shows the prediction accuracy of the gray-box model over $100\tau_R$ with an initial condition and input sequence not used during training, i.e., testing data. A video of the test data comparison is shown in Movie S1. Fig. 2a shows the L^2 norm of the error between the predicted and measured number densities with x-marks marking when the actuator changes. Fig. 2b-e show snapshots of the test trajectory with columns [1-6] corresponding to $t = [0\tau_R, 20\tau_R, 40\tau_R, 60\tau_R, 80\tau_R, 99\tau_R]$, respectively. Column 1 shows the initial conditions for n . Fig. 2b shows snapshots of the particle simulation. Note the entire simulation has a height of about 50ℓ so we show only a subsection. Particles are colored to indicate their orientation: purple for right-oriented particles and green for left-oriented particles. Orientation is determined by the normalized polar order in x , defined as $m_x(x)/n(x)$, where $m_x(x) = \int \int \cos(\theta) P(\mathbf{x}, \theta, t) d\theta dy$. Positive values of $m_x(x)/n(x)$ correspond to right-oriented particles (purple), while negative values correspond to left-oriented particles (green). Regions without strong polar order are colored white. Colored arrows above are to guide the eye. Fig. 2c shows measured (blue) and predicted (red) snapshots of the density n . Fig. 2d shows the measured (blue) and predicted (red) flux due to velocity field $v_x n$. We emphasize that the gray-box model learns v based on the density field dynamics $n(x, t)$ as input data, rather than directly using the measured values of v . Fig. 2e shows the actuator at the time of the snapshot.

As can be seen in Fig. 2a, the error norm remains below 0.01 and this corresponds to a number density profile that closely resembles the measured density profile as seen in Fig. 2b. Furthermore, there are no sudden increases in the error norm when the input field changes, suggesting the dynamics are well captured.

Turning our attention to the advective flux in Fig. 2d, despite never explicitly providing the measured flux to the gray-box model, we can see by matching the number density, the gray-box model also matches the advective flux throughout the test simulation, minus the fluctuations induced by the multibody particle collisions and thermal noise. These results demonstrate that the gray-box model accurately captures both the number density and emergent flux behavior, validating its suitability for implementation within the MPC framework.

IV. MODEL PREDICTIVE CONTROL (MPC)

The concept of MPC is to optimize a user-defined objective subject to the model dynamics and system constraints, e.g., the maximum induced velocity the actuator can apply. Formally, provided initial conditions n_0 and p_0 , we solve the following nonlinear optimization problem to find the optimal control sequence $\underline{\Omega}^o$ over a control time horizon K , minimizing over the sequence of inputs,

$\underline{\Omega}$:

$$\begin{aligned}
& \min_{\underline{\Omega}} \sum_{k=0}^{K-1} L(\hat{n}(k), \underline{\Omega}(k)) + L_f(\hat{n}(K)) \\
& \text{s.t. } \hat{n}(k+1) = f_h(\hat{n}(k), \underline{\Omega}(k), v_{\text{NN}}(\hat{n}(k), \underline{\Omega}(k), \hat{p}(k); \beta_{\text{NN}})), \\
& \quad \hat{p}(k+1) = f_p(\hat{n}(k), \underline{\Omega}(k), \hat{p}(k)), \\
& \quad \hat{n}(0) = n_0, \\
& \quad \hat{p}(0) = p_0, \\
& \quad \underline{\Omega}(k) \subseteq \mathbb{W} \quad \forall k \in [0, K-1]
\end{aligned} \tag{11}$$

$\underline{\Omega}(k)$ is the k th element of the sequence $\underline{\Omega}$; $L(\cdot)$ is the stage cost and $L_f(\cdot)$ is the terminal cost; $f_p(\cdot)$ is a sliding window function that drops the oldest element of the past vector $\hat{p}(k)$ and appends the newest elements, namely, $\hat{n}(k)$ and $\underline{\Omega}(k)$; The stage cost is typically chosen to penalize the deviation of the number density from the set point $n_{\text{sp}}(x, t)$ and the control effort. As discussed before, the predicted trajectory typically deviates from the realized trajectory due to model errors or system perturbations and thus, feedback is required to correct the actuator sequence. This is achieved by solving the optimization problem at each sample time $h\tau_{\text{R}}$ and applying the first element of the optimal control sequence to the system as shown in Fig. 1c. To solve this nonlinear optimization problem at each sample time, we implement the solution using IPOPT within the CasADI framework [70–72].

We demonstrate the gray-box MPC framework using two examples. In the first, we split the population into two groups and dynamically juggle the densities between them, showcasing precise control over spatial distributions. In the second, we simultaneously regulate the number density and the mean flux, guiding the mean flux to follow a prescribed sinusoidal profile while maintaining the particle groups at their target positions. For both examples, we consider a control horizon $K = 14$, i.e., a control horizon of $7\tau_{\text{R}}$, and a sample time $h = 0.5\tau_{\text{R}}$.

The splitting example is shown in Movie S2, and the simultaneous control of density and mean flux is demonstrated in Movie S3. Additional examples are provided to highlight the framework’s versatility. In Movie S4, we again show the results for Movie S2, but include the MPC forecast. In Movie S5, we revisit the splitting example but reformulate the stage cost using the Wasserstein distance, illustrating how the framework can fit particles to arbitrary distributions [73]. In Movie S6, we design the fastest trap of width 4ℓ moving to the right that keeps 60% of the particles in the trap. Code is available at https://github.com/titusswsquah/graybox_abp_mpc [74].

V. SPLITTING AND JUGGLING THE POPULATION

For all the examples, we initialize the simulations with the particles accumulated at the center. The user set points are as follows:

1. Split particles into two equal groups centered at $x_+ = 2.5\ell$ and $x_- = -2.5\ell$, where $\ell = U_0\tau_{\text{R}}$ is the run length.
2. Achieve a distribution where the probability of finding a particle with position $x < 0$ is 30% while maintaining the populations centered at x_{\pm} .
3. Repeat step 2, but with the probability of finding a particle with position $x < 0$ is 70%.
4. Return to step 1.

A. Notation

The operator $\langle \cdot \rangle$ denotes the expectation of its argument over the entire domain, evaluated using number density $n(x, t)$, i.e.,

$$\langle \cdot \rangle = \int (\cdot) n(x, t) dx$$

To represent the probability of finding a particle in the right half of the domain, we define $n(x > 0) = \langle H(x) \rangle$. Similarly, the probability of finding a particle in the left half of the domain is denoted as $n(x < 0)$. The operator $\langle \cdot \rangle_{\mathcal{D}}$ denotes the expectation of its argument over sub-domain \mathcal{D} , also evaluated using number density $n(x, t)$. For example, the expectation restricted to the right half of the domain is expressed as:

$$\langle \cdot \rangle_{x>0} = \frac{\langle (\cdot) H(x) \rangle}{n(x > 0)}$$

B. Stage cost formulation

With these definitions, we are ready to define the stage cost $L_1(\cdot)$.

$$L_1(n(x, t), r_{\text{sp}}(t)) = c_1(L_+ + L_-) + c_2L_r \tag{12}$$

$$L_- = \left\langle (x - x_-)^2 \right\rangle_{x < 0} \tag{13}$$

$$L_+ = \left\langle (x - x_+)^2 \right\rangle_{x > 0} \tag{14}$$

$$L_r = (n(x < 0) - r_{\text{sp}}(t)n(x > 0))^2 \tag{15}$$

In the stage cost $L_1(\cdot)$, we penalize only number density deviations, as opposed to also penalizing a control effort. The cost L_1 consists of three contributions. L_- penalizes the expected square distance of particles to the left of the origin ($x < 0$) to the left set point x_- . Likewise, L_+ penalizes the expected square distance of particles to the right of the origin ($x > 0$) to the right set point x_+ . The last term in the distribution cost L_r penalizes deviations from the left-to-right ratio set point $r_{\text{sp}}(t)$ between probability of finding a particle to the left $n(x < 0)$ and right $n(x > 0)$ of the origin. This ratio penalty is used

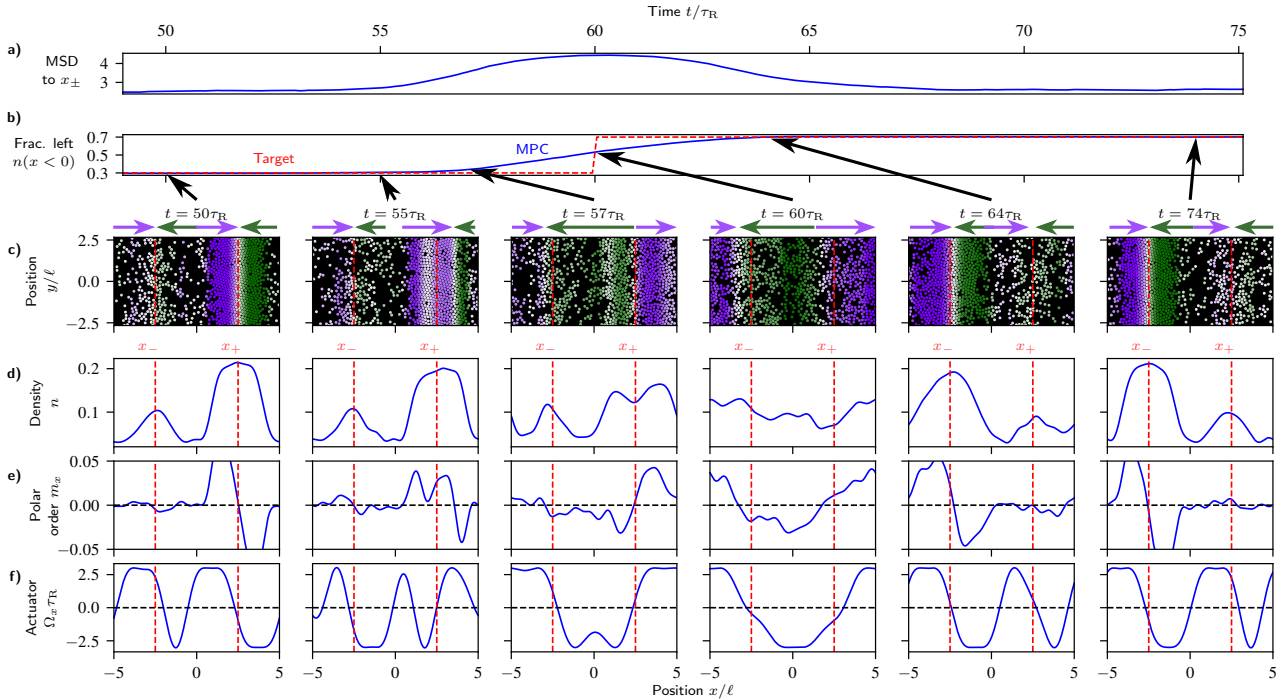


FIG. 3. Control of number density using gray-box MPC. behavior during the transition from step 2 to step 3, where particles are transferred from the x_+ to the x_- group. The steps are as follows: (1) Split particles into two equal groups centered at x_+ and x_- ; (2) Achieve a distribution where 30% of the particles are to the left of the origin while maintaining the populations centered at x_+ and x_- ; (3) Repeat step 2 with 70% of the particles to the left of the origin; and (4) Return to step 1. The set point change occurs at $t = 60\tau_R$, and the time interval $[50\tau_R, 75\tau_R]$ is analyzed. (a) The sum of the mean squared distances (MSDs) of particles to their respective set points, x_+ and x_- , is plotted. (b) The target fraction of particles to the left of the origin (red line) and the realized fraction under Model Predictive Control (MPC) (blue line) are shown. (c) Snapshots of the particle simulation at six key time points: $t = 50\tau_R$, $55\tau_R$, $57\tau_R$, $60\tau_R$, $64\tau_R$, and $74\tau_R$. Particles are colored based on their expected orientation in the x direction, averaged over the y direction: purple indicates particles oriented to the right, green indicates particles oriented to the left, and white indicates no strong orientation. Red dashed lines mark the set points x_+ and x_- . Colored arrows above the particles guide the eye. (d) Snapshots of the number density field at the same six time points. (e) Snapshots of the polar order field. (f) The actuating field applied to the system, extracted from the first input in the MPC sequence, is displayed. We refer to points where the actuator field switches from positive to negative as attractive wells and locations where the field switches from negative to positive as repulsive hills. Notice that in preparation for the set point change at $t = 60\tau_R$, the controller begins planning at $t = 53\tau_R$ and takes action by orienting particles in the x_+ group leftward (green) while jamming particles near the x_+ set point to maintain proximity. This behavior creates a pressure front, preparing the particles for transfer to x_- while preventing excessive displacement from x_+ .

to achieve set points like equal-sized groups or 30% of particles to the left.

The weights for the positional set point penalty and the ratio penalty are chosen to be $c_1 = 1$ and $c_2 = 100$, respectively. c_2 was chosen large since the scale of the ratio penalties are much smaller compared to the positional set point penalties. The terminal cost L_f is chosen to be the same as L_1 . A movie of the full process is shown in Movie S2.

C. Controller behavior

We examine the transition from step 2 to step 3, focusing on the transfer of particles from the x_+ to the x_- group as shown in Fig. 3. The set point change occurs at $t = 60\tau_R$, and we analyze the controller's behavior during the time interval $[50\tau_R, 75\tau_R]$. Fig. 3a displays the combined costs of maintaining populations at x_{\pm} , repre-

sented by the sum of mean squared distances between the left (right) particles and x_- (x_+). In Fig. 3b, we compare the target fraction (red) and MPC-realized fraction of particles to the left of $x = 0$. The lower panels present simulation snapshots at six time points: $t = 50\tau_R$, $55\tau_R$, $57\tau_R$, $60\tau_R$, $64\tau_R$, and $74\tau_R$.

Fig. 3c illustrates the particle simulation snapshots, with particles colored according to their expected orientation along the x -axis, averaged over the y direction. Purple indicates rightward orientation, green indicates leftward orientation, and white indicates no strong directional preference. Guiding arrows above the particles highlight these orientations, while red dashed lines mark the set points x_{\pm} . The remaining panels show complementary measurements: Fig. 3d presents the density field, Fig. 3e displays the polar order, and Fig. 3f shows the actuator field applied to the system, derived from the

initial input of the MPC sequence.

At the beginning of the interval, particles are distributed around their respective set points, with the left particles clustered near x_- and right particles near x_+ . The simulation snapshot at $t = 50\tau_R$ in Fig. 3c and the corresponding density profile in Fig. 3d show a smaller population near the left set point, maintaining the target fraction of $n(x < 0) \approx 0.3$. The controller’s behavior, illustrated in Fig. 3f, directs the particles toward the set points. Specifically, the field transitions from positive to negative values, creating “attractive wells” near the set points. Conversely, transitions from negative to positive values generate “repulsive hills”, which appear at the simulation cell boundaries ($x = \pm 5\ell$) and at the center ($x = 0$). These repulsive regions effectively channel particles away from these locations and toward the designated set points. The effectiveness of this orienting field is evident in Fig. 3e, where the polar order parameters exhibit characteristic transitions from positive to negative values in the vicinity of x_{\pm} , confirming the controlled directional behavior of the particles.

Recall we are using a control horizon of $7\tau_R$, so for the upcoming set point change occurring at $t = 60\tau_R$, the controller begins planning at $t = 53\tau_R$. At this point, the controller initiates action through a sophisticated approach that leverages two fundamental features of the active hard disks system: the limited actuator field and jamming dynamics. Due to the constraints of the limited actuator field, the controller cannot instantaneously reorient particles from the right group to the left group. Instead, from $t = 53\tau_R$ to $t = 56\tau_R$, the controller methodically prepares the particles by orienting the majority of particles in the x_+ group toward the left, as evidenced by their green coloration in the $t = 55\tau_R$ simulation snapshot (Fig. 3c). This reorientation, however, presents a challenge: the particles’ self-propulsion causes them to move rightward once oriented in that direction. The controller addresses this through a strategic jamming mechanism, directing a layer of particles (displayed in purple) to the left of the group to move rightward, thereby opposing the main group’s flux. This creates an effective pressure front that serves two purposes: preparing the particles for their leftward migration while maintaining their position near the x_+ set point. This preparation phase is apparent in both the polar order (Fig. 3d) and the actuating field (Fig. 3e). The controller maintains an attractive well at x_- while establishing a more complex structure around x_+ : a repulsive hill flanked by two attractive wells that effectively jam the particles to prevent escape. The polar order reveals a transition from positive to negative values to the left of the x_+ set point. Notably, the number density shown in Fig. 3d remains relatively unchanged compared to the $t = 50\tau_R$ snapshot, a consistency that is reflected in the minimal variations observed in both the sum of MSDs (Fig. 3a) and the left fraction (Fig. 3b).

From $t = 56\tau_R$ to $t = 61\tau_R$, the controller floods particles leftward, transferring them from x_+ to x_- as shown

in the $t = 57\tau_R$ and $t = 60\tau_R$ snapshots (Fig. 3c,d). This transfer is driven by an attractive well at x_- and a repulsive hill at x_+ in both the polar order and actuating field (Fig. 3e,f). During this period, the sum of MSDs increases, peaking at $t = 60\tau_R$ (Fig. 3a), while the left fraction approaches its 70% set point (Fig. 3b). From $t = 61\tau_R$ to $t = 75\tau_R$, the controller directs particles to their respective set points, maintaining attractive wells at both x_- and x_+ (Fig. 3e,f). The left fraction reaches its 70% set point by $t = 64\tau_R$ (Fig. 3b), and the controller continues minimizing the sum of MSDs until $t = 69\tau_R$ (Fig. 3a).

VI. ADVECTIVE FLUX CONTROL

In the previous example, we focused solely on controlling the number density. Given the gray-box model’s accurate prediction of advective flux, we now extend our approach to simultaneously control both the advective flux and number density. We maintain the two-population particle system accumulated near x_{\pm} while introducing control of the system’s mean flux ψ to follow a sinusoidal profile:

$$\psi_{\text{sp}}(t) = \psi_{\text{max}} \sin\left(\frac{2\pi}{T}t\right) \quad (16)$$

where ψ_{max} is the target flux magnitude, and T is the period. The stage cost extends Eq. (12) by adding a term that penalizes deviations between realized and set point mean fluxes.

$$L_2(n(x, t), \psi_{\text{sp}}(t)) = L_1(n(x, t)) + L_{\psi} \quad (17)$$

$$L_{\psi} = c_3 (\psi - \psi_{\text{sp}}(t))^2, \quad \psi = \frac{\langle v_x \rangle}{W} \quad (18)$$

ψ represents the mean flux (i.e., flux averaged over the domain); c_3 is the weight for the velocity penalty. The terminal cost L_f is chosen to be L_1 . Since the percentage of particles in the left or right half is not relevant in this example, we set $c_2 = 0$.

We set $\psi_{\text{max}} = 0.01\ell/\tau_R$, $T = 20\tau_R$, $c_1 = 1$, and $c_3 = 10^3$. Starting with particles equally split into two populations, we simulate the system for $20\tau_R$. A full process visualization is provided in Movie S3, while key snapshots are presented in Fig. 4. The set point flux (dashed red line) and measured flux (solid blue line) are shown in panel (a). Panels (b)-(e) illustrate simulation snapshots of particle positions (with green/purple arrows indicating leftward/rightward polar order), density, flux (dashed red for the set point, solid blue for measured mean, and blue shaded line for field), and the actuating field. Red dashed vertical lines mark target particle accumulation positions.

At the simulation’s start ($t = 0$), the two populations are equally distributed about x_{\pm} , oriented roughly towards x_{\pm} , as depicted by the particles and their colors in Fig. 4b. This configuration corresponds to density peaks at x_{\pm} in Fig. 4c. The initial set point mean flux is zero, and the gray-box MPC successfully achieves this flux, as

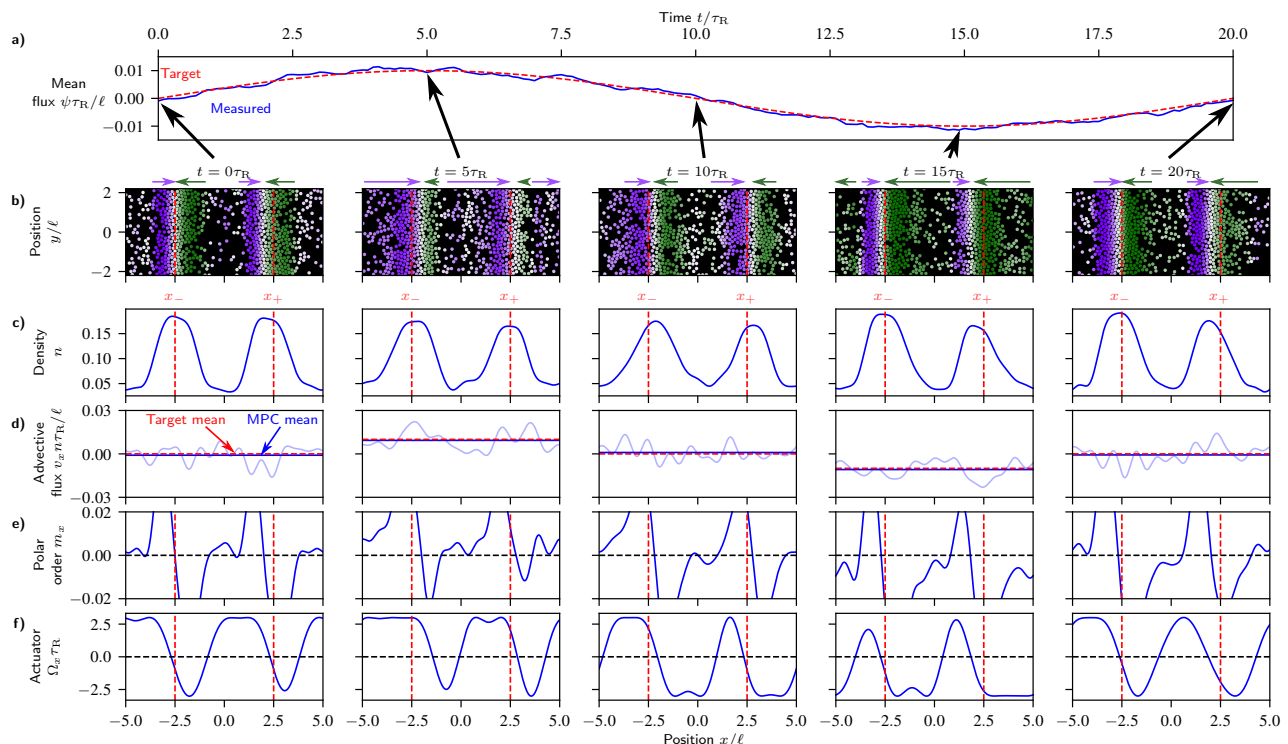


FIG. 4. Simultaneous control of particle number density and mean flux using gray-box MPC. (a) The set point mean flux (dashed red line) and measured flux (solid blue line) show accurate tracking throughout the sinusoidal profile. (b) Particle positions and polar order at representative times, highlighting leftward (green) and rightward (purple) orientations. (c) Density profiles consistently accumulate near x_{\pm} , indicating the successful maintenance of the target accumulation. (d) Flux profiles confirm precise mean flux control, with measured mean flux (solid blue line) matching the set point (dashed red line). (e) Actuator field snapshots reveal dynamic control strategies, including field modulation to achieve target fluxes, paired with localized jamming around x_{\pm} to maintain density accumulation about x_{\pm} . Red dashed vertical lines indicate target particle accumulation points, emphasizing the controller’s ability to simultaneously regulate both number density and flux across the domain.

evidenced by the dashed red and solid blue lines overlapping in Fig. 4d. The actuator initially behaves as it does when splitting the populations, creating two attractive wells at x_{\pm} . The repulsive hills are shifted left to start directing particles to the right, as the target flux begins to increase.

By $t = 5\tau_R$, the set point mean flux reaches its maximum value of 0.01. The gray-box MPC accurately tracks the set point, as shown in Fig. 4d. To achieve this, the controller directs most particles to the right, indicated by the purple particles in Fig. 4b and the positive actuator field over most of the domain in Fig. 4e. Despite this flux, the density remains accumulated near x_{\pm} , as seen in Fig. 4c. To maintain density accumulation at x_{\pm} , the controller creates a jam at x_{\pm} by redirecting particles to the right of x_{\pm} leftwards. This behavior ensures that particles stay localized near x_{\pm} while the desired mean flux is achieved. This is evident from the green particles on the right of x_{\pm} in Fig. 4b and the negative actuator field to the right of x_{\pm} in Fig. 4e.

The simulation follows a similar pattern in the opposite direction. At $t = 10\tau_R$, the particles regroup near x_{\pm} with zero mean flux. At $t = 15\tau_R$, the set point

flux reaches its minimum value of -0.01. The gray-box MPC achieves this flux by applying a predominantly negative field across the domain, directing particles leftward. Again, to jam the particles about x_{\pm} , the controller creates an opposing group to the left of x_{\pm} , directing them rightward with a positive field, resulting in the desired mean flux. Throughout, particles remain concentrated near x_{\pm} . Finally, at $t = 20\tau_R$, the simulation concludes with particles gathered near x_{\pm} and zero mean flux. This strategy demonstrates the ability to simultaneously control number density and advective flux.

VII. DISCUSSION

In this work, we have developed and demonstrated a gray-box MPC framework for active matter systems, focusing on interacting ABPs. Using physics-informed machine learning, we accurately modeled the dynamics of the number density and integrated this predictive model into an MPC framework to control emergent behaviors. We validated the framework with two illustrative examples: splitting the population into two groups and dynamically juggling their densities, and simultaneously controlling both the number density and the mean flux

to follow a sinusoidal profile. These results highlight the framework’s ability to handle complex, multi-objective control tasks in active matter systems, demonstrating both accuracy and flexibility.

While our focus in this work was on learning the advective operator, there are natural extensions for cases where learning the diffusion operator is also critical. For example, in the Stokes limit, where hydrodynamics are governed by Stokes equations, particles exhibit long-range interactions due to flow fields induced by their motion. In such systems, the diffusion operator becomes a mobility tensor that depends on the system’s configuration, requiring a closure relation that accounts for the number density, actuator inputs, and their histories [75]. Similarly, the fluctuations in the density field motivates exploring stochastic partial differential equations (PDEs). This exploration can build upon existing work on stochastic physics-informed neural ordinary differential equations (ODEs) [76] by extending their methodology to PDEs through established numerical techniques like spectral methods and the method of lines. These techniques enable the transformation of PDEs into systems of ODEs, allowing us to learn the moments of the number density and velocity while leveraging the original framework’s capabilities for handling stochastic elements.

Looking beyond this study, our framework has the potential to impact experimental systems, such as light-activated bacteria or other active colloidal systems, where bacteria density dynamics can be learned and controlled [20, 22]. Additionally, the framework’s focus on learning dynamics and closures from data suggests appli-

cations in entirely different domains, such as improving continuum traffic models for urban planning and vehicle coordination [77].

Ultimately, this work highlights the promise of combining physics-informed machine learning with MPC to tackle the complexity of active matter systems. By bridging the gap between data-driven methods and physical principles, our approach addresses a long-standing challenge in the field: systematic control of emergent behaviors. With its ability to adapt to disturbances and optimize multi-objective tasks, this framework represents a scalable and versatile tool for future research and applications in active matter and beyond.

VIII. ACKNOWLEDGMENTS

We would like to thank Steven J. Kuntz and Sachit G. Nagella for helpful discussions. T.Q. is supported by the National Science Foundation Graduate Research Fellowship Program under Grant No. 2139319. S.C.T. is supported by the Packard Fellowship in Science and Engineering. Use was made of computational facilities purchased with funds from the National Science Foundation (CNS-1725797) and administered by the Center for Scientific Computing (CSC). The CSC is supported by the California NanoSystems Institute and the Materials Research Science and Engineering Center (MRSEC; NSF DMR 2308708) at UC Santa Barbara.

Code availability. Code is available at https://github.com/titussswsquah/graybox_abp_mpc [74].

Supplementary Information

CONTENTS

A. Methods	1
1. Gray-box modeling	1
2. Training data	1
3. Training protocol	2
4. Learning the advective flux	2
5. Orthogonal series estimation	3
References	5

Appendix A: Methods

1. Gray-box modeling

Following [78, 79], we consider a forced dynamical system of the form

$$\dot{X} = F(X(t), \Omega(t)) \quad (\text{A1})$$

F describes dynamics of the full state X and the actuator input Ω . Now suppose we cannot directly measure $X(t)$ but rather some function of the full state $n(t) = H(X(t))$, $H(\cdot)$ is the measurement function, and we would like to develop a dynamical model for the measurable $n(t)$. Furthermore, we have knowledge of some physics that constrain how $n(t)$ can evolve, e.g. conservation laws or symmetry, expressed as $f(\cdot)$.

$$\dot{n}(t) = f(n(t), \Omega(t), v(X(t), \Omega(t))) \quad (\text{A2})$$

$v(X(t), \Omega(t))$ is the unknown function of the full state $X(t)$ that evolves the dynamics of n exactly. However, we can only measure $n(t)$ which may only be a partial measurement of the full state. Motivated by Taken's embedding theorem, we introduce a delay embedding $p(t) = [n(t-h), \Omega(t-h), \dots, n(t-(N_p-1)h), \Omega(t-(N_p-1)h)]^T$ where h is the sampling time and N_p is the embedding dimension [68]. We assume that there exists an estimator Ψ that estimates the full state $X(t)$ from the measurement $n(t)$ and its past $p(t)$. For practical usage, N_p is heuristically chosen to provide a reasonable fit to the data. Thus, we can rewrite Eq. (A2) as

$$\dot{n}(t) = f(n(t), \Omega(t), \hat{v}(n(t), \Omega(t), p(t))) \quad (\text{A3})$$

where the last unknown is the function $\hat{v}(\cdot)$ that handles both the estimation of the full state with estimator Ψ and evaluates the effect of the full state on the state of interest $n(t)$. Thus, we approximate $\hat{v}(\cdot)$ with a parameterized function approximator, namely a feedforward artificial neural network $v_{\text{NN}}(n(t), \Omega(t), p(t); \beta_{\text{NN}})$ where β_{NN} are the network parameters.

$$\dot{n}(t) = f(n(t), \Omega(t), v_{\text{NN}}(n(t), \Omega(t), p(t); \beta_{\text{NN}})) \quad (\text{A4})$$

This gray-box modeling framework naturally extends to partial differential equations through a combination of spectral methods and the method of lines [80]. Specifically, spectral methods allow us to represent the spatial components of the PDE using basis functions with time-varying coefficients. The method of lines then transforms the PDE into a system of ODEs governing these spectral coefficients. In this setting, the neural network becomes a neural operator that maps the current and past spectral coefficients (through the delay embedding) to their future evolution, while maintaining the physics-informed structure through $f(\cdot)$.

2. Training data

With measurements of $n(t)$ available at sampling time h and zero-order hold applied to Ω_x , we can represent this as a discrete-time dynamical system with time step k . For simplicity, we refer to the measurement at time k as $n(k)$ and the actuator input at time k as $\Omega_x(k)$. The model is designed to accurately represent both transient dynamics and

steady-state behavior. The control input is subject to constraints $\|\Omega_x(\mathbf{x}, t)\|_\infty \leq \Omega_{\max}$. To systematically explore the actuator field's capabilities up to the maximum magnitude Ω_{\max} , we employ spatial collocation at uniform intervals in x . At these collocation points, we sample the actuator field values uniformly from the interval $[-\Omega_{\max}, \Omega_{\max}]$. At the initial time step and at the end of each hold period, we iterate the following:

1. Sample new input values at collocation points uniformly from $[-\Omega_{\max}, \Omega_{\max}]$, and a new hold duration k_h uniformly from integers in $[k_{\min}, k_{\max}]$.
2. Hold the actuator input constant at Ω_x for the next k_h time steps, or until total time steps $k_f + N_p$, while recording both the number density $n(k)$ and input $\Omega_x(k)$ at each step.

At the end of data collection, we have a trajectory of measurements and inputs which we split into initial conditions for the past $p_0 = (n(0), \Omega_x(0), \dots, n(N_p - 1), \Omega_x(N_p - 1))$ and the training trajectory number densities $\underline{n} = (n(N_p), \dots, n(N_p + k_f))$ and inputs $\underline{\Omega} = (\Omega_x(N_p), \dots, \Omega_x(k_f + N_p - 1))$.

We repeat this process for N_{traj} trajectories to obtain a dataset of initial conditions and training trajectories.

3. Training protocol

For clarity, we introduce the multi-step prediction error minimization approach with a single trajectory. To obtain the unknown parameters β_{NN} , we minimize the squared norm between the measured and predicted trajectories.

$$\begin{aligned} \min_{\beta_{\text{NN}}} \quad & \sum_{k=0}^{k_f} \|\underline{n}(k) - \hat{n}(k)\|^2 \\ \text{s.t.} \quad & \hat{n}(k+1) = f_h(\hat{n}(k), \underline{\Omega}(k), v_{\text{NN}}(\hat{n}(k), \underline{\Omega}(k), p(k); \beta_{\text{NN}})), \\ & \hat{p}(k+1) = f_p(\hat{n}(k), \underline{\Omega}(k), \hat{p}(k)), \\ & \hat{n}(0) = \underline{n}(0), \\ & \hat{p}(0) = p_0 \end{aligned}$$

where $f_h(\cdot)$ is the discrete time dynamics of the number density n obtained via numerical integration of Eq. (A4) with step size h , e.g., a Runge Kutta method; $f_p(\cdot)$ is a sliding window function that drops the oldest element of the past vector $\hat{p}(k)$ and appends the newest elements, namely, $\hat{n}(k)$ and $\underline{\Omega}(k)$; In other words, provided initial conditions and the input sequence, a predicted trajectory is generated by integrating the gray-box model Eq. (A4) with the estimated parameters β_{NN} and the error between the predicted and measured trajectories is minimized by updating the parameters β_{NN} . This approach has been shown to increase the long time accuracy as compared to a single step approach, i.e. $\min_{\beta_{\text{NN}}} \sum_{k=0}^{k_f-1} |\underline{n}(k+1) - f(\underline{n}(k), \underline{\Omega}(k), v_{\text{NN}}(\underline{n}(k), \underline{\Omega}(k), \underline{p}(k); \beta_{\text{NN}}))|^2$ [54, 81]. For N_{traj} trajectories, we minimize the sum of the trajectory errors to find the optimal parameters β_{NN} .

4. Learning the advective flux

We numerically approximate the advection-diffusion equation Eq. (8) using spectral methods.

$$\begin{aligned} \dot{\mathbf{n}} &= -\iota \mathbf{K} (-D_T \iota \mathbf{K} + \mathbf{T} v_{\text{NN}}(\mathbf{n}, \boldsymbol{\Omega}, \mathbf{p}; \beta_{\text{NN}})) \mathbf{n} \\ &:= \mathbf{F}(v_{\text{NN}}(\mathbf{n}, \boldsymbol{\Omega}, \mathbf{p}; \beta_{\text{NN}})) \mathbf{n} \end{aligned}$$

$\mathbf{n} \in \mathbb{R}^{d_n}$ is the vector of Fourier coefficients for the number density; $\boldsymbol{\Omega} \in \mathbb{R}^{d_\Omega}$ is vector of actuator field coefficients; $\mathbf{p} \in \mathbb{R}^{N_p(d_n + d_\Omega)}$ is the vector of past number density and actuator field coefficients; $v_{\text{NN}}(\cdot) : \mathbb{R}^{(N_p+1)(d_n + d_\Omega)} \rightarrow \mathbb{R}^{d_v}$ is the neural network that maps the number density, actuator coefficients, and the past density and actuator coefficients to the velocity field coefficients and is parameterized by β_{NN} ; \mathbf{K} is the Fourier differentiation matrix; \mathbf{T} is the rank 3 tensor that Toeplitzizes the neural network output $v_{\text{NN}}(\cdot)$ for convolution with \mathbf{n} .

Provided N_{traj} trajectories of length k_f with initial number density and past vectors, we minimize the sum of

trajectory errors to find the optimal parameters β_{NN} :

$$\min_{\beta_{\text{NN}}} \sum_{i=1}^{N_{\text{traj}}} \sum_{k=1}^{k_f} |\mathbf{n}_i(k) - \hat{\mathbf{n}}_i(k)|^2 \quad (\text{A5a})$$

$$\text{s.t.} \quad \hat{\mathbf{n}}_i(k+1) = \hat{\mathbf{n}}_i(k) + h\mathbf{F}(\hat{\mathbf{v}}(k))\hat{\mathbf{n}}_i(k+1), \quad (\text{A5b})$$

$$\hat{\mathbf{v}}(k) = \mathbf{v}_{\text{NN}}(\hat{\mathbf{n}}_i(k), \underline{\boldsymbol{\Omega}}_i(k), \hat{\mathbf{p}}_i(k); \beta_{\text{NN}}), \quad (\text{A5c})$$

$$\hat{\mathbf{p}}_i(k+1) = (\hat{\mathbf{n}}_i(k), \underline{\boldsymbol{\Omega}}_i(k), \hat{\mathbf{p}}_i^{0:N_p-2}(k)), \quad (\text{A5d})$$

$$\hat{\mathbf{n}}_i(0) = \mathbf{n}_i(0), \quad (\text{A5e})$$

$$\hat{\mathbf{p}}_i(0) = \mathbf{p}_{i,0} \quad (\text{A5f})$$

ι is the imaginary number; $\mathbf{n}_i(k)$ and $\hat{\mathbf{n}}_i(k)$ are the measured and predicted density trajectory for the k th step of the i th trajectory, respectively; $\underline{\boldsymbol{\Omega}}_i(k)$ is the input at the k th step in the i th trajectory; $\hat{\mathbf{p}}_i(k)$ is the predicted past vector at step k of the i th trajectory; $\mathbf{p}_{i,0}$ is the initial past density and input coefficients for the i th trajectory.

Eq. (A5a) is the sum of squared errors between the predicted and measured number density trajectories; Eq. (A5b) is the numerical integration of the advection-diffusion equation with a modified backward Euler method; Eq. (A5c) is the neural network approximation for the effective velocity; Eq. (A5d) describes the sliding window for the past coefficients; $\hat{\mathbf{p}}_i^{0:N_p-2}$ is the vector of past coefficients excluding the oldest set of coefficients; Eqs. (A5e) and (A5f) are the initial conditions for the number density and past coefficients, respectively.

Note the diffusion operator is stiff, which requires either small time steps or an implicit solver. We would like large time steps for control, which motivates an implicit solver. Thus, the numerical integration of the advection-diffusion equation is done using a modified backward Euler method where the nonlinear term is evaluated using only the current time step. This allows Eq. (A5b) to be linear in $\hat{\mathbf{n}}_i(k+1)$. This approach is analogous to an implicit-explicit method where nonlinear non-stiff portions are evaluated explicitly while linear stiff operations are handled implicitly. Rather than have a separate dynamical system for \mathbf{v}_{NN} which we evolve separately, we simply use the past to predict the future velocity field which minimizes errors in number density trajectories. The main motivation for the modified approach is to avoid tracking gradients through an iterative nonlinear solver. With the implicit-explicit approximation, solving Eq. (A5b) requires a single Newton step as the problem is linear. Alternatively, adjoint sensitivities could be used, but we found the modified backward Euler method to be faster for our problem [82]. Alternatively, one could leverage the implicit function theorem to define the solver's dynamics in terms of its sensitivity to inputs and directly compute gradients for optimization [83].

We used $N_{\text{traj}} = 1000$, $k_f = 20$, $N_p = 2$, $d_n = d_v = 21$, $d_\Omega = 11$, $h = 0.5\tau_R$, $k_{\text{min}} = 5$ and $k_{\text{max}} = 20$. For the neural network, we used a single-layer feedforward neural network with 64 nodes and hyperbolic tangent activation functions. Optimization was done using the Adam optimizer in PyTorch with a learning rate of 10^{-3} .

In addition to the training data, we used a validation set of 100 trajectories to monitor the training process. More specifically, we used the validation set to monitor the loss function and if the validation loss did not decrease for 20 epochs, we stopped training.

Lastly, the testing data, i.e., data not used during any part of training, we chose to evaluate the model on $N_{\text{test}} = 100$ trajectories of length $k_f = 200$. We evaluated a longer trajectory to ensure the model had long time prediction capabilities.

5. Orthogonal series estimation

We use an orthogonal series estimator to estimate the density. Suppose you have a random variable x with density $n(x)$ and you wish to estimate $n(x)$ from N samples $[x_1 \ x_2 \ \cdots \ x_N]^T$. We use the following estimator.

$$\hat{n}(x) = \sum_{j=-d}^d \hat{a}_j P_j(x)$$

$$\hat{a}_j = \frac{1}{N \|P_j\|^2} \sum_{i=1}^N P_j(x_i)$$

$\hat{n}(x)$ is the orthogonal series estimate; $P_j(x)$ being the j th orthogonal basis function; \hat{a}_j being the j th coefficient. d is the degree of the orthogonal series. In other words, the true coefficients are the expected value of the basis functions, i.e., $a_j = \langle P_j(x) \rangle$, so we estimate the coefficients by averaging over the samples.

This can also be used to estimate averages of observable quantities $A(x)$, e.g., fluxes or polar orders.

$$\hat{A}(x) = \sum_{j=-d}^d \hat{a}_{A,j} P_j(x)$$

$$\hat{a}_{A,j} = \frac{1}{N \|P_j\|^2} \sum_{i=1}^N P_j(x_i) A_i$$

A_i is the observable quantity for sample i . For the examples in the main paper, we use a Fourier basis, i.e., $P_j(x) = e^{2\pi i j x/W}$. To handle confinement in examples in the SI, we use Legendre polynomials.

-
- [1] M. C. Marchetti, J. F. Joanny, S. Ramaswamy, T. B. Liverpool, J. Prost, M. Rao, and R. A. Simha, *Rev. Mod. Phys.* **85**, 1143 (2013).
- [2] H. Chaté, *Annu. Rev. Condens. Matter Phys.* **11**, 189 (2020).
- [3] C. Bechinger, R. Di Leonardo, H. Löwen, C. Reichhardt, G. Volpe, and G. Volpe, *Rev. Mod. Phys.* **88**, 045006 (2016).
- [4] R. A. Simha and S. Ramaswamy, *Phys. Rev. Lett.* **89**, 058101 (2002).
- [5] S. Ramaswamy, *Annu. Rev. Condens. Matter Phys.* **1**, 323 (2010).
- [6] A. Sciortino and A. R. Bausch, *Proc. Natl. Acad. Sci. USA* **118**, e2017047118 (2021).
- [7] T. Vicsek, A. Czirók, E. Ben-Jacob, I. Cohen, and O. Shochet, *Phys. Rev. Lett.* **75**, 1226 (1995).
- [8] S. Thampi and J. Yeomans, *Eur. Phys. J.: Spec. Top.* **225**, 651 (2016).
- [9] J. Tailleur and M. E. Cates, *Phys. Rev. Lett.* **100**, 218103 (2008).
- [10] R. Zhang, S. A. Redford, P. V. Ruijgrok, N. Kumar, A. Mozaffari, S. Zemsky, A. R. Dinner, V. Vitelli, Z. Bryant, M. L. Gardel, and J. J. de Pablo, *Nat. Mat.* **20**, 875 (2021).
- [11] A. M. Tayar, F. Caballero, T. Anderberg, O. A. Saleh, M. Cristina Marchetti, and Z. Dogic, *Nat. Mat.* **22**, 1401 (2023).
- [12] D. Grober, I. Palaia, M. C. Uçar, E. Hannezo, A. Šarić, and J. Palacci, *Nat. Phys.* , 1 (2023).
- [13] S. Ramananarivo, E. Ducrot, and J. Palacci, *Nat. Commun.* **10**, 1 (2019).
- [14] T. Zhou, X. Wan, D. Z. Huang, Z. Li, Z. Peng, A. Anandkumar, J. F. Brady, P. W. Sternberg, and C. Daraio, *Sci. Adv.* **10**, eadj1741 (2024).
- [15] P. Guillamat, J. Ignés-Mullol, and F. Sagués, *Proc. Natl. Acad. Sci. USA* **113**, 5498 (2016).
- [16] J. Palacci, S. Sacanna, A. P. Steinberg, D. J. Pine, and P. M. Chaikin, *Science* **339**, 936 (2013).
- [17] M. A. Fernandez-Rodriguez, F. Grillo, L. Alvarez, M. Rathlef, I. Buttinoni, G. Volpe, and L. Isa, *Nat. Commun.* **11**, 1 (2020).
- [18] S. Palagi, D. P. Singh, and P. Fischer, *Adv. Opt. Mat.* **7**, 1900370 (2019).
- [19] I. Buttinoni, G. Volpe, F. Kümmel, G. Volpe, and C. Bechinger, *J. Phys. Condens. Matter* **24**, 284129 (2012).
- [20] G. Frangipane, D. Dell’Arciprete, S. Petracchini, C. Maggi, F. Saglimbeni, S. Bianchi, G. Vizsnyiczai, M. L. Bernardini, and R. Di Leonardo, *eLife* **7**, e36608 (2018).
- [21] L. M. Lemma, M. Varghese, T. D. Ross, M. Thomson, A. Baskaran, and Z. Dogic, *PNAS Nexus* **2**, pgad130 (2023).
- [22] J. Arlt, V. A. Martinez, A. Dawson, T. Pilizota, and W. C. K. Poon, *Nat. Commun.* **9**, 768 (2018).
- [23] J. Arlt, V. A. Martinez, A. Dawson, T. Pilizota, and W. C. K. Poon, *Nat. Commun.* **10**, 2321 (2019).
- [24] S. C. Takatori, R. De Dier, J. Vermant, and J. F. Brady, *Nat. Commun.* **7**, 1 (2016).
- [25] T. Mano, J. B. Delfau, J. Iwasawa, and M. Sano, *Proc. Natl. Acad. Sci. USA* **114**, E2580 (2017).
- [26] A. F. Demirörs, M. T. Akan, E. Poloni, and A. R. Studart, *Soft Matt.* **14**, 4741 (2018).
- [27] M. Fränzl and F. Cichos, *Sci. Rep.* **10**, 12571 (2020).
- [28] N. Pellicciotta, M. Paoluzzi, D. Buonomo, G. Frangipane, L. Angelani, and R. Di Leonardo, *Nat. Commun.* **14**, 4191 (2023).
- [29] H. Massana-Cid, C. Maggi, G. Frangipane, and R. Di Leonardo, *Nat. Commun.* **13**, 2740 (2022).
- [30] M. Baldovin, D. Guéry-Odelin, and E. Trizac, *Phys. Rev. Lett.* **131**, 118302 (2023).
- [31] N. Koumakis, A. T. Brown, J. Arlt, S. E. Griffiths, V. A. Martinez, and W. C. K. Poon, *Soft Matt.* **15**, 7026 (2019).
- [32] S. Shankar, L. V. D. Scharrer, M. J. Bowick, and M. C. Marchetti, *Proc. Natl. Acad. Sci. USA* **121**, e2400933121 (2024).
- [33] K. Nishiyama, J. Berezney, M. M. Norton, A. Aggarwal, S. Ghosh, M. F. Hagan, Z. Dogic, and S. Fraden, Closed-loop control of active nematic flows (2024), arXiv:2408.14414 [cond-mat, physics:physics].
- [34] M. M. Norton, P. Grover, M. F. Hagan, and S. Fraden, *Phys. Rev. Lett.* **125**, 178005 (2020).
- [35] C. Sinigaglia, F. Braghin, and M. Serra, *Phys. Rev. Lett.* **132**, 218302 (2024).
- [36] L. K. Davis, K. Proesmans, and E. Fodor, *Phys. Rev. X* **14**, 011012 (2024).
- [37] S. Shankar, V. Raju, and L. Mahadevan, *Proc. Natl. Acad. Sci. USA* **119**, e2121985119 (2022).
- [38] S. Ghosh, A. Baskaran, and M. F. Hagan, Achieving designed texture and flows in bulk active nematics using optimal control theory (2024), arXiv:2408.14596 [cond-mat.soft].
- [39] S. Ghosh, C. Joshi, A. Baskaran, and M. F. Hagan, Spatiotemporal control of structure and dynamics in a polar active fluid (2024).
- [40] J. B. Rawlings, D. Q. Mayne, and M. M. Diehl, *Model Predictive Control: Theory, Design, and Computation*, 2nd ed. (Nob Hill Publishing, Santa Barbara, CA, 2020) 770 pages, ISBN 978-0-9759377-5-4.
- [41] S. J. Qin and T. A. Badgwell, *Control Eng. Pract.* **11**, 733 (2003).
- [42] S. Yu, M. Hirche, Y. Huang, H. Chen, and F. Allgöwer, *Auton. Intell. Syst.* **1**, 4 (2021).
- [43] A. Shenoy, C. V. Rao, and C. M. Schroeder, *Proc. Natl. Acad. Sci. USA* **113**, 3976 (2016).
- [44] R. Wittkowski, A. Tiribocchi, J. Stenhammar, R. J. Allen, D. Marenduzzo, and M. E. Cates, *Nat. Commun.* **5**, 4351 (2014).
- [45] M. t. Vrugt, J. Bickmann, and R. Wittkowski, *J. Phys. Condens. Matter* **35**, 313001 (2023).
- [46] E. J. Hinch and L. G. Leal, *J. Fluid Mech.* **76**, 187 (1976).
- [47] B. Ezhilan, M. J. Shelley, and D. Saintillan, *Phys. Fluids* **25**, 070607 (2013).
- [48] S. Weady, M. J. Shelley, and D. B. Stein, *J. Comput. Phys.* **457**, 110937 (2022).
- [49] M. Raissi, P. Perdikaris, and G. E. Karniadakis, *J. Comput. Phys.* **378**, 686 (2019).
- [50] G. E. Karniadakis, I. G. Kevrekidis, L. Lu, P. Perdikaris, S. Wang, and L. Yang, *Nat. Rev. Phys.* **3**, 422 (2021).
- [51] S. L. Brunton, J. L. Proctor, and J. N. Kutz, *Proc. Natl. Acad. Sci. USA* **113**, 3932 (2016).

- [52] Z. Li, H. Zheng, N. Kovachki, D. Jin, H. Chen, B. Liu, K. Azizzadenesheli, and A. Anandkumar, Physics-Informed Neural Operator for Learning Partial Differential Equations (2023).
- [53] M. Golden, R. O. Grigoriev, J. Nambisan, and A. Fernandez-Nieves, *Sci. Adv.* **9**, eabq6120 (2023).
- [54] S. Maddu, S. Weady, and M. J. Shelley, *J. Comput. Phys.* **504**, 112869 (2024).
- [55] C. Joshi, S. Ray, L. M. Lemma, M. Varghese, G. Sharp, Z. Dogic, A. Baskaran, and M. F. Hagan, *Phys. Rev. Lett.* **129**, 258001 (2022).
- [56] R. Supekar, B. Song, A. Hastewell, G. P. T. Choi, A. Mietke, and J. Dunkel, *Proc. Natl. Acad. Sci. USA* **120**, e2206994120 (2023).
- [57] J. Colen, M. Han, R. Zhang, S. A. Redford, L. M. Lemma, L. Morgan, P. V. Ruijgrok, R. Adkins, Z. Bryant, Z. Dogic, M. L. Gardel, J. J. de Pablo, and V. Vitelli, *Proc. Natl. Acad. Sci. USA* **118**, e2016708118 (2021).
- [58] S. Sanyal and K. Roy, in *2023 IEEE International Conference on Robotics and Automation (ICRA)* (2023) pp. 1019–1025.
- [59] Y. Zheng, C. Hu, X. Wang, and Z. Wu, *J. Proc. Cont.* **128**, 103005 (2023).
- [60] P. Kumar, J. B. Rawlings, M. J. Wenzel, and M. J. Risbeck, *Energ. Buildings* **286**, 112936 (2023).
- [61] M. E. Cates and J. Tailleur, *Annu. Rev. Condens. Matter Phys.* **6**, 219 (2015).
- [62] J. A. Anderson, J. Glaser, and S. C. Glotzer, *Comput. Mater. Sci.* **173**, 109363 (2020).
- [63] J.-P. Hansen and I. R. McDonald, *Theory of Simple Liquids: with Applications to Soft Matter* (Academic Press, 2013).
- [64] D. Saintillan and M. J. Shelley, *C. R. Phys.* **14**, 497 (2013).
- [65] J. Jeggle, J. Stenhammar, and R. Wittkowski, *J. Chem. Phys.* **152**, 194903 (2020).
- [66] J. Bickmann, S. Bröker, M. te Vrugt, and R. Wittkowski, *Phys. Rev. E* **108**, 044601 (2023).
- [67] A. Frishman and P. Ronceray, *Phys. Rev. X* **10**, 021009 (2020).
- [68] F. Takens, in *Dynamical Systems and Turbulence*, Lecture Notes in Mathematics, Vol. 398, edited by D. A. Rand and L.-S. Young (Springer, 1981) p. 366–381.
- [69] N. N. Cencov, *Sov. Math. Dokl.* **3**, 1559 (1962).
- [70] A. Wächter and L. T. Biegler, *Math. Prog.* **106**, 25 (2006).
- [71] J. A. E. Andersson, J. Gillis, G. Horn, J. B. Rawlings, and M. Diehl, *Math. Prog. Comp.* **11**, 1 (2019).
- [72] M. J. Risbeck and J. B. Rawlings, MPCTools: Nonlinear model predictive control tools for CasADi (Python interface) (2015).
- [73] C. Villani, *Optimal transport: old and new*, Vol. 338 (Springer, 2009).
- [74] T. Quah, S. C. Takatori, and J. B. Rawlings, Code for “Physics-informed Neural Model Predictive Control of Interacting Active Brownian Particles” (2025).
- [75] G. J. Elfring and J. F. Brady, *J. Fluid Mech.* **952**, A19 (2022).
- [76] J. O’Leary, J. A. Paulson, and A. Mesbah, *J. Comput. Phys.* **468**, 111466 (2022).
- [77] D. G. Patsatzis, L. Russo, I. G. Kevrekidis, and C. Siettos, *J. Comput. Phys.* **478**, 111953 (2023).
- [78] R. J. Lovelett, J. L. Avalos, and I. G. Kevrekidis, *Ind. Eng. Chem. Res.* **59**, 2611 (2019).
- [79] P. Kumar and J. B. Rawlings, *Comput. Chem. Eng.* **177**, <https://doi.org/10.1016/j.compchemeng.2023.108314> (2023).
- [80] R. G. Patel, N. A. Trask, M. A. Wood, and E. C. Cyr, *Comp. Meth. Appl. Mech. Eng.* **373**, 113500 (2021).
- [81] T. Askham and J. N. Kutz, *SIAM J. Appl. Dyn. Syst.* **17**, 380 (2018).
- [82] R. T. Chen, Y. Rubanova, J. Bettencourt, and D. K. Duvenaud, *Adv. Neural Inf. Process. Syst.* **31** (2018).
- [83] A. Look, S. Doneva, M. Kandemir, R. Gemulla, and J. Peters, arXiv preprint arXiv:2010.07078 (2020).